

A Terahertz Signal Transmission in Plasma Sheath with Different Vehicle Size

Zhikang Chu¹, Mingyang Mao², Jiawei Xiong³, Ziyang Zhao^{4,*}, Rongxin Tang⁴, and Kai Yuan^{1,4}

¹*School of Information Engineering, Nanchang University, Nanchang 330031, China*

²*School of Resources and Environment, Nanchang 330031, China*

³*School of Physics and Materials Science, Nanchang 330031, China*

⁴*Institute of Space Science and Technology, Nanchang University, Nanchang 330038, China*

ABSTRACT: Communication blackout is a serious threat to aerospace engineering. Over the past decade, the terahertz (THz) technology has been considered an effective solution to the blackout problem. However, it is currently unclear that how the size of the vehicle affects the conditions of the THz communication channel within the plasma sheath. In this study, a numerical hypersonic hydrodynamical model is introduced to investigate the relationship between THz signal attenuation in the plasma sheaths and the size of the vehicle. The analysis shows that the size of the vehicle significantly influences the structure of the plasma sheath. The thickness of the plasma sheath increases linearly with the size of the vehicle. The maximum electron density in smaller vehicles shows unstable fluctuations, attributed to variations in size causing changes in the flow velocity and mass density, resulting in the variation of pressure distribution. Additionally, with the increase of plasma sheath thickness, the attenuation coefficient of THz signals increases linearly. Therefore, for the vehicles of large sizes, the designs that minimize the thickness of the plasma sheath are helpful to mitigate the communication blackout.

1. INTRODUCTION

When a spacecraft is flying at hypersonic speeds in the atmosphere, the air in front of the spacecraft is compressed, creating shock-waves and causing a rapid increase in temperature. This phenomenon leads to the ionization of the surrounding gas, forming a plasma. This plasma layer is referred to as the plasma sheath, containing a significant number of free electrons. It severely disrupts the transmission of radio wave signals, a phenomenon commonly known as the blackout phenomenon [1]. Communication blackout can occur during a certain phase of the flight, causing the spacecraft to lose contact with ground control stations and other communication nodes, resulting in communication interruptions [2]. This situation not only impacts mission execution but also poses a threat to spacecraft safety [3, 4].

Global researchers have been tirelessly seeking methods to eliminate or mitigate the communication barriers caused by the plasma sheath. Strategies proposed to date include optimizing the vehicle's configuration to reduce plasma formation on the vehicle's surface, thereby lowering communication interference [5]. The ablation material method involves incorporating metal oxides into the vehicle's thermal protection materials [6]. When the thermal protection material ablates, the metal oxides neutralize electrons in the plasma, reducing electron density. The magnetic window technique utilizes an external magnetic field to adjust the distribution of electrons on the vehicle's surface, altering the propagation characteristics of electromagnetic waves in the plasma sheath and thereby enhancing the permeability of communication signals [7, 8]. The method of inject-

ing electron-affinitive liquids involves introducing electron-affinitive liquids into the plasma sheath to facilitate the recombination of electrons and ions, reducing electron density and effectively alleviating communication blackout issues [9]. The high and low-frequency method refers to significantly reducing the attenuation coefficient of plasma when the electromagnetic wave frequency is much lower or higher than the plasma frequency [10]. Relay methods avoid directly weakening or eliminating the plasma sheath [11]. Instead, they leverage its uneven spatial distribution by transmitting electromagnetic waves from the thinner regions of the sheath to relay stations or relay satellites, and finally to the ground, bypassing the severe attenuation of direct transmission to the ground. However, these methods face technical or practical limitations, such as cost, system weight, and aerodynamic performance. In recent decades, terahertz communication with operating frequencies between 0.1 THz and 10 THz has been regarded as a potential solution to address communication blackout issues [12, 13].

The transmission characteristics of terahertz signals in the plasma sheath layer have been studied through theoretical and experimental research [14]. Dong et al. [15] investigated the transmission characteristics of terahertz waves in the plasma sheath of hypersonic targets. Zhang and Guohua [16] also analyzed the impact of random plasma distribution on the transmission characteristics of THz waves. Tian et al. [17] found that collisions between electrons and neutral particles play a crucial role in the attenuation of extremely high-frequency signals within the plasma sheath layer. Rao et al. [18] examined the impact of electron density and electron collision frequency on the attenuation of extremely high-frequency signals in the plasma sheath layer, noting that this attenuation inten-

* Corresponding author: Ziyang Zhao (zhaozy006@ncu.edu.cn).

TABLE 1. Definitions of Variables, all variables are in SI units.

ρ : Mass Density	t : Time	n : Number Density
P : Pressure	e : Total Energy	m : Mass
R : Gas Constant	T : Temperature	μ : Dynamic Viscosity
1-3 H : Heat Generation	σ : Silicon Collision Diameter	K_T : Thermal Conductivity
Ω : Collision Integral	K_B : Boltzmann Constant	P_r : Prandtl Number
f : Degrees of Freedom	N : Total Number of Species	s : Specific Source
ν_e : Electron Collision Frequency	γ : c_P/c_V	γ : c_P/c_V
c_V : Specific Heat at Constant Volume	\vec{u} : Fluid Velocity	i : Subscript, i -th Species
$\vec{\tau}$: Viscous Stress Tensor	\vec{I} : Unit Tensor	R_i : Gas constant of the i -th component

sifies with their increase. Zhang et al. [19] pointed out that the spatial distribution of plasma also affects the attenuation of extremely high-frequency signals within the plasma sheath. Zhang et al. [20] simulated the process of electromagnetic wave penetration through a nonuniform reentry plasma sheath layer. Changes in flight conditions may result in variations in the attenuation of terahertz signals, as these conditions affect electron density and electron collision frequency [21]. Additionally, Wei et al. [22] noted that signal attenuation changes over time along with variations in the plasma sheath. Methods to reduce the attenuation of terahertz signals in the plasma sheath layer include adjusting the angle of attack proposed by Chen et al. [23], changing the spacecraft velocity suggested by Tang et al. [24], and introducing an external magnetic field to modulate the dispersion characteristics of extremely high-frequency waves proposed by Guo et al. [25]. Ouyang et al. [26] also studied the differences in the propagation of terahertz waves in the thermal-chemical non-equilibrium plasma sheath of different hypersonic vehicle shapes.

Previous studies have significantly advanced our understanding of terahertz wave transmission in reentry plasma sheath layers. These studies have analyzed the time-varying characteristics of vehicle plasma sheath and proposed various approaches to enhance terahertz signal transmission. However, these investigations were based on the assumption that the size and shape of hypersonic vehicle are fixed. Nevertheless, the considerable variations in vehicle size and shape, and their impact on the structure and internal characteristics of the plasma sheath, have not been adequately explored. To effectively address the communication blackout problem, it is crucial to consider the influence of vehicle size on the plasma sheath layer and terahertz wave transmission. This study aims to focus on this issue.

This paper begins by employing hypersonic fluid dynamics theory to numerically simulate the reentry plasma sheath of hypersonic vehicle of various sizes [27]. Subsequently, data obtained from the hypersonic fluid model is utilized to analyze the transmission characteristics of terahertz signal in an actual plasma sheath. Scattering Matrix Method (SMM) is employed to simulate the transmission of terahertz waves in the plasma sheaths of different-sized veh. Subsequently, data obtained from the hypersonic fluid model is utilized to analyze the transmission characteristics of terahertz signal in an actual plasma sheath. SMM is employed to simulate the transmission

of terahertz waves in the plasma sheaths of different-sized vehicles [28].

2. INFLUENCE OF VARIOUS VEHICLE SIZES ON PLASMA SHEATH

The study adopts the dimensions of the RAMC-II blunt vehicle as a baseline, characterized by a top spherical radius of 15.24 cm, a cone angle of 9° , a major axis length of 1.29 m, a flight altitude of 61 km, and a velocity of 6550 m/s [29]. To investigate the impact of size variations on the sheath, the vehicle is proportionally scaled while keeping other variables constant. The chosen scaling range is from 0.5 to 10, with the major axis length ranging from 0.645 m to 12.9 m, covering the dimensions of existing hypersonic vehicle [30].

The present study conducts a comprehensive simulation analysis of the plasma sheath generated by high-speed aircraft, employing principles of fluid dynamics and numerical computation techniques. By accounting for the compressibility of fluids, the complexity of chemical reactions, and employing advanced numerical methods, a more precise prediction of the behavior and characteristics of the plasma sheath is achieved.

The model assumes the plasma sheath to be a compressible Newtonian fluid, disregarding higher-order terms of viscosity and microfluidic effects. It does not consider the influence of geomagnetic fields and electromagnetic waves on the distribution of electron density, nor does it incorporate the effects of acceleration and deceleration of the aircraft on the structure of the sheath. The model is primarily based on the Navier-Stokes equations, expressed as follows [31, 32]:

$$\frac{\partial \rho}{\partial t} + \nabla \cdot (\rho \vec{u}) = 0 \quad (1)$$

$$\frac{\partial (\rho \vec{u})}{\partial t} + \nabla \cdot \left(\rho \vec{u} \otimes \vec{u} + p \vec{I} \right) = \nabla \cdot \vec{\tau} + \rho \vec{g} \quad (2)$$

$$\frac{\partial e}{\partial t} + \nabla \cdot (e \vec{u}) = -\nabla \cdot \left(p \vec{u} + \vec{q} - \vec{u} \cdot \vec{\tau} \right) \quad (3)$$

Equations (1) through (3) represent respectively the mass equation, momentum equation, and energy equation within the Naive-Stokes equation system, where all variables are defined as shown in Table 1. Here, ρ denotes the mass density, $\rho =$

$\sum_i^N n_i m_i$; n_i represents the number density of the i th species of particles; m_i stands for the mass of the i th species of particles. In Equation (3), the three terms on the right-hand side respectively denote the contributions of pressure gradient, heat conduction, and viscosity forces to the rate of change of energy.

The expression for the viscous stress tensor is obtained through the following equation, where T represents the transpose operator of the matrix:

$$\vec{\tau} = -\frac{2}{3}\mu(\nabla \cdot \vec{u})\vec{I} + \mu[\nabla \otimes \vec{u} + (\nabla \otimes \vec{u})^T] \quad (4)$$

The total energy in the Navier-Stokes equations comprises internal energy, kinetic energy, and chemical energy, as given by Equation (5), where the heat flux is determined by Fourier's law:

$$e = \frac{p}{\gamma - 1} + \frac{1}{2}\rho\vec{u} \cdot \vec{u} + \sum_i^N n_i H_i \quad (5)$$

$$\vec{q} = -k_T \nabla T \equiv -c_P \frac{\mu}{Pr} \nabla T \quad (6)$$

Under the assumptions of this model, any potential influence of geomagnetic fields and electromagnetic waves on the electron density within the sheath is disregarded. Additionally, the dynamic changes (acceleration or deceleration) of the aircraft affecting the sheath structure are not considered, thus rendering the volume force term as zero. Based on these assumptions, Equations (2) and (3) are simplified and reformulated as follows:

$$\frac{\partial(\rho\vec{u})}{\partial t} + \nabla \cdot (\rho\vec{u} \otimes \vec{u} + p\vec{I}) = \nabla \cdot \vec{\tau} \quad (7)$$

$$\frac{\partial e}{\partial t} + \nabla \cdot [\vec{u}(e + p)] = \nabla \cdot (\vec{\tau} \cdot \vec{u}) + \nabla \cdot (k_T \nabla T) \quad (8)$$

Furthermore, to achieve closure of the Navier-Stokes equation system describing the fluid dynamics model in this framework, namely Equations (1), (7), and (8), the equation for number density of particles needs to be introduced [33, 32]:

$$\frac{\partial n_i}{\partial t} + \nabla \cdot (n_i \vec{u}) = s_i \quad (9)$$

$$-\mu_i = \frac{5}{16} \frac{\sqrt{\pi m_i k_B T}}{\pi \sigma^2 \Omega} \quad (10)$$

$$c_{Pi} = \left(\frac{f}{2} + 1\right) R_i \quad (11)$$

$$c_{Vi} = c_{Pi} - R_i \quad (12)$$

$$k_{Ti} = \frac{5}{2} c_{Vi} \mu_i \quad (13)$$

In Equation (9), the term on the right-hand side represents the source term, which accounts for the chemical reactions within the plasma sheath. In this study, the NASA Standard Seven-Component Air Model is employed for investigation [34]. The

seven chemical components involved in the chemical reactions are: N_2 , N , O_2 , O , NO , NO^+ , and e^- .

Before solving the plasma sheath of the spacecraft using fluid dynamics models, it is necessary to finely partition the spacecraft into unstructured tetrahedral meshes to optimize the accuracy and stability of the simulation. Fig. 1 illustrates the grid partition when the size ratio of vehicles (SRV = 1) is 1, with the color bar on the right indicating the size of the mesh areas. In the subsequent parts of this study, the "size ratios of vehicles" is abbreviated as SRV.

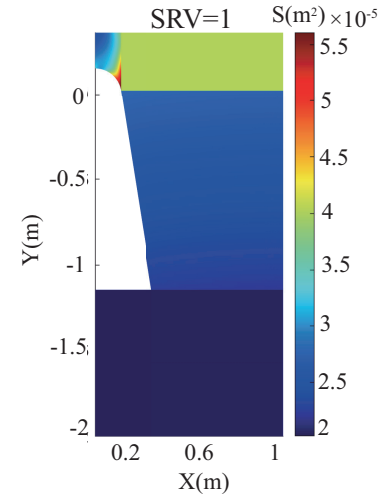


FIGURE 1. The mesh partitioning for an aircraft size ratio of 1 is displayed in Fig. 1, where different colors represent the size of the partitioned mesh areas.

Unstructured tetrahedral meshes mainly consist of quadrilaterals of similar dimensions, aiming to present the mesh as parallelograms as much as possible to reduce numerical oscillations. This grid design takes into account the complexity of adapting to geometric shapes near the spacecraft, especially in cases of significant gradients of physical quantities and curvature of the spacecraft outline. In regions far from the spacecraft, rectangular meshes were chosen in this study to match different simulation scale requirements and simplify the calculation process.

Due to the significant gradients of physical quantities within the plasma sheath and the curvature of the spacecraft outline, this model employs the finite volume method (FVM) in unstructured tetrahedral meshes [35, 36]. In FVM, the computational domain is divided into a set of control volumes, with each volume center having a representative node. By integrating conservation-type partial differential equations, a discrete equation system is obtained, and numerical methods are then used to solve these equations to compute the physical quantities at each control volume center. This method ensures the satisfaction of conservation laws while also accommodating the computational aspects of the nonlinear characteristics of the plasma sheath to achieve stable and accurate simulation results.

Considering the axisymmetric design characteristics of hypersonic aircraft, the plasma sheath surrounding it naturally exhibits the same symmetrical properties. This symmetry significantly simplifies the analysis process of the plasma sheath, so in this study, information about the entire sheath is obtained by

studying half of the spacecraft sheath structure. This approach reduces computational complexity and requires computational resources while retaining a comprehensive understanding of the entire sheath.

Through the aforementioned grid partitioning and fluid dynamics models, different-sized spacecraft plasma sheath structures can be obtained. The simulation results depict the two-dimensional distribution of the aircraft plasma sheath within the specified region, including parameters such as electron density, temperature, and pressure, as shown in Fig. 2.

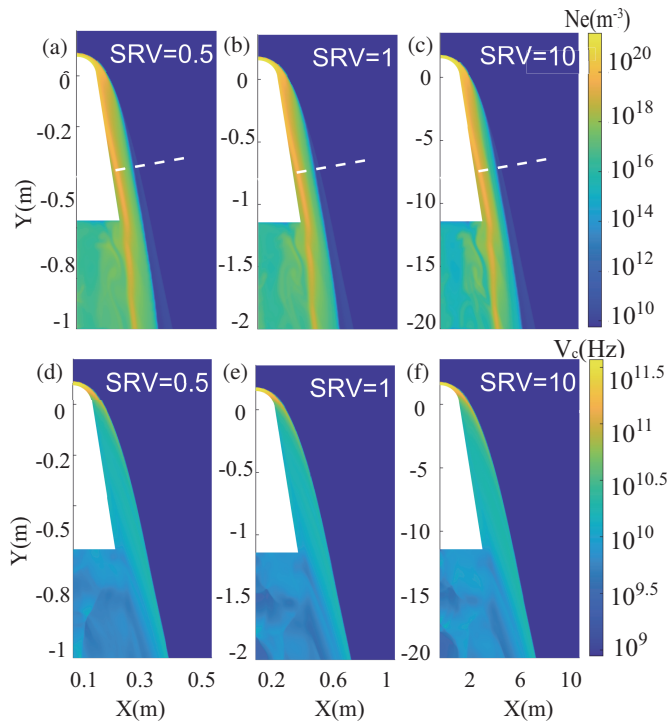


FIGURE 2. (a) represents the electron density for a size ratio of 0.5, (b) for a size ratio of 1, and (c) for a size ratio of 10. (d) represents the electron collision frequency for a size ratio of 0.5, (e) for a size ratio of 1, and (f) for a size ratio of 10. The white dashed lines in Figs. (a)–(c) represent the signal transmission path.

Figure 2 illustrates the distribution of electron density within the plasma sheaths for size ratios of vehicles of 0.5, 1, and 10 (a)–(c), as well as the distribution of collision frequency between electrons and neutral particles (d)–(f). The collision frequency is obtained from (14) [37]:

$$\nu_c = 3 \times 10^8 \left(\frac{\rho}{\rho_0} \right) T \quad (14)$$

where ρ is the mass density, T the temperature, and $\rho_0 = 1.28823 \text{ kg/m}^3$.

From Fig. 2, it is evident that the distribution of the plasma sheath is highly nonuniform and changes in vehicle size (VS) result in corresponding variations in electron density and collision frequency. In the vehicle with a size ratio of 1, the top electron density is significantly higher than in other regions, and the plasma in the wake region is less uniformly distributed than in the sidewall region. Additionally, regardless of changes

in SRV, the plasma parameters in the sidewall region are relatively more stable than the wake region and the top. Therefore, installing antennas on the sidewall is advantageous for maintaining a stable communication channel. In this study, the communication path is located near the sidewall approximately 3/4 from the top of the corresponding sized vehicles, indicated by the white dashed line in Figs. 2(a)–(c). By calculating the sheath thickness along the transmission path for different size ratios, Fig. 3 intuitively illustrates the relationship between sheath thickness and SRV.

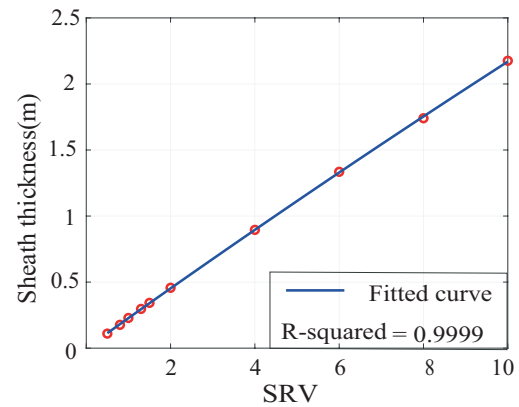


FIGURE 3. The variation pattern of spacecraft size ratio and sheath thickness is depicted, with red circles representing the original data points and a blue curve representing the curve fitted data. Additionally, the R-squared value is annotated on the graph.

The horizontal axis of Fig. 3 represents the SRV, and the vertical axis displays the sheath thickness along the signal transmission path. Fitting the data reveals that, with an increase in SRV, the sheath thickness around it exhibits a linear growth, with a slope value of 0.2286. This change significantly impacts the physical characteristics of the sheath. The model-fitted data achieved a high R-squared value of 0.9999, indicating a remarkably close fit to the actual observed values and confirming the predictive capability of the model. Furthermore, the distribution characteristics of electron density along the electromagnetic wave propagation path and the specific distribution of electron collision frequency will be explored in detail, as shown in Fig. 4.

In Fig. 4(a), the distribution of electron density (solid line) and electron collision frequency (dashed line) along the wave transmission path for an SRV of 1 is presented, with the normalized distance to the antenna on the horizontal axis. The electron density along the wave transmission path exhibits a Gaussian function characteristic, and the electron collision frequency along the path has three sequentially increasing peaks. Figs. 4(b) and (c) depict the distributions of electron density and collision frequency along the transmission path for size ratios of 0.5, 1, and 10. The electron density along the wave propagation path in different-sized vehicle follows a Gaussian distribution, and the maximum electron density consistently occurs at a distance of approximately 0.162 from the antenna. Additionally, the distribution of electron collision frequency shows a similar trend across all sizes, displaying three peaks at positions 0.02, 0.55, and 0.89 in distance from the antenna.

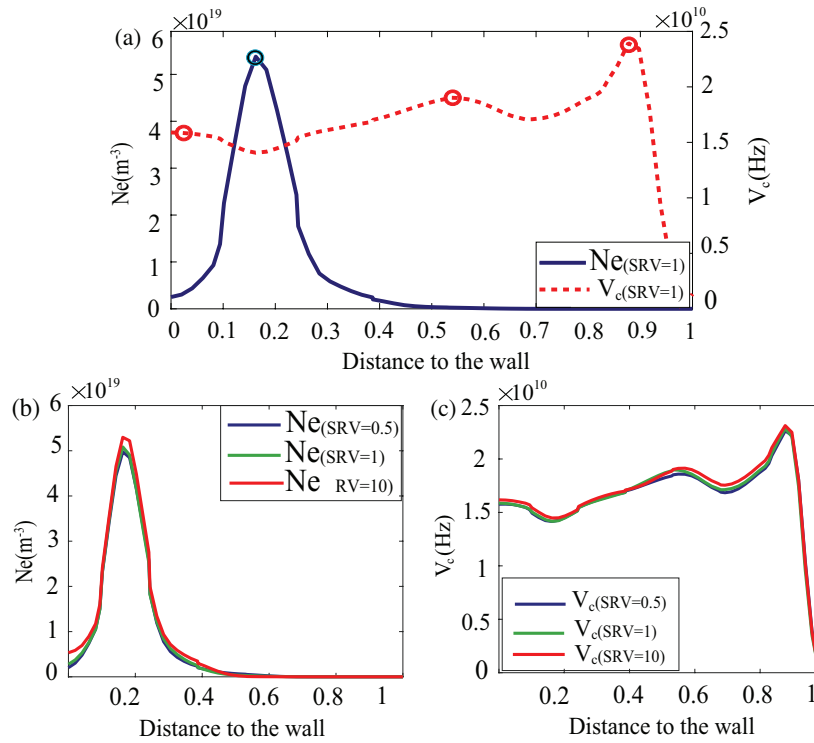


FIGURE 4. Distribution of electron density and electron collision frequency along the wave transmission path at the SRV of 1(a), and (b) electron density and (c) electron collision frequency along the transmission path for different sizes.

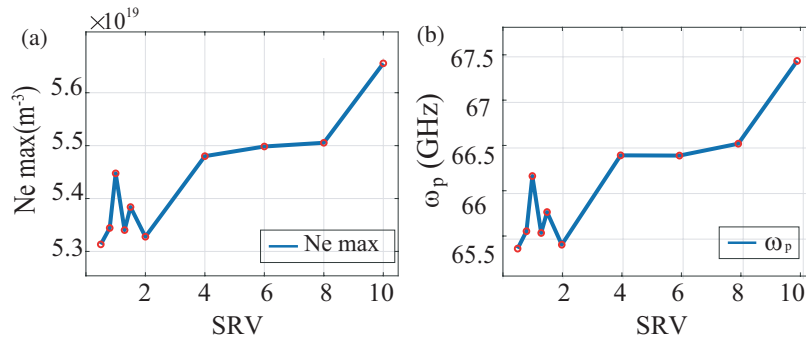


FIGURE 5. (a) Variation in maximum electron density and (b) cutoff frequency along the transmission path with SRV.

While the position of the maximum electron density along the propagation path remains consistent across all size ratios, there are numerical differences at various sizes. Fig. 5 reveals the relationship between the maximum electron density and cutoff frequency with the SRV.

Fig. 5(a) displays the numerical values of the maximum electron density along the transmission path. Fig. 5(b) illustrates the relationship between the cutoff frequency along the transmission path and the SRV, calculated using (2) [38]:

$$\omega_p = \sqrt{\frac{n_e e^2}{\varepsilon_0 m_e}} \quad (15)$$

where e is the elementary charge of an electron, m_e the electron mass, and ε_0 the relative permittivity of vacuum.

The cutoff frequency, as indicated by Formula (2), is directly associated with the electron density in the environment and de-

pends solely on this single variable. Moreover, Fig. 5 reveals that the cutoff frequency and maximum electron density exhibit the same changing trend. Therefore, investigating the reasons for the variation in maximum electron density can explain the changes in the cutoff frequency. At a size ratio of 0.5, the maximum electron density reaches $N_{e \text{ max}} = 5.31 \times 10^{19} \text{ m}^{-3}$, while at a size ratio of 10, its value is $5.65 \times 10^{19} \text{ m}^{-3}$, with the corresponding cutoff frequency fluctuating within the range of 65.11 GHz to 67.47 GHz. As the SRV increases from 2 to 10, the maximum electron density along the transmission path shows an increasing trend. However, when the ratio increases from 0.5 to 2, the electron density changes unpredictably, exhibiting a piece-wise-linear pattern. This change will be discussed in detail next.

The variation in electron density is influenced by the evolution of the plasma sheath and affected by various environmen-

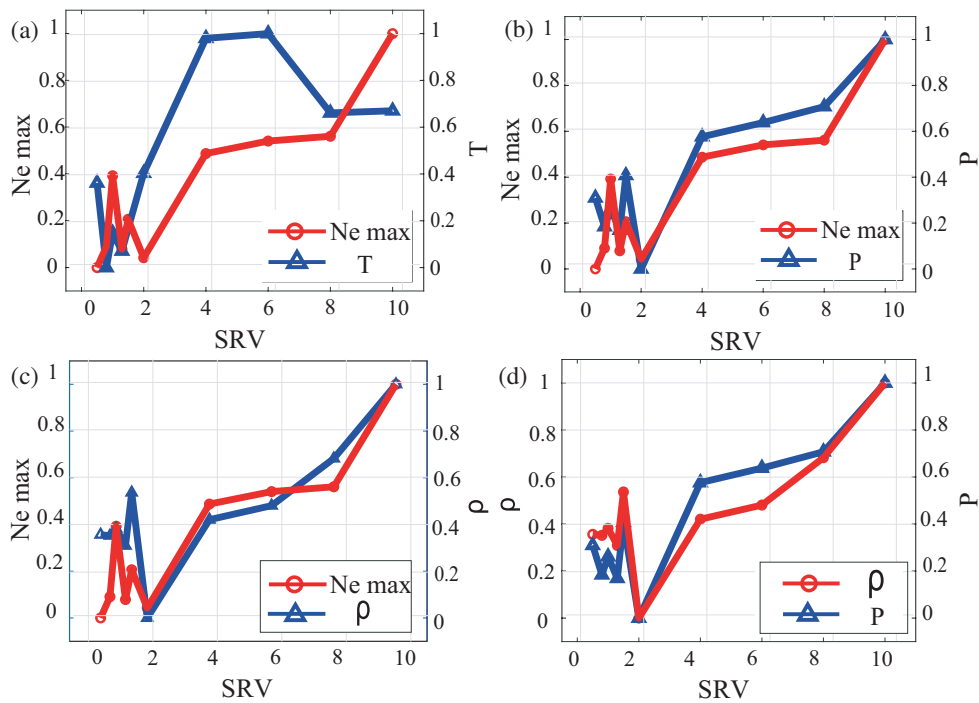


FIGURE 6. Comparative trends of (a) temperature, (b) pressure, (c) mass density, and maximum electron density near the antenna with SRV, and (d) comparative trends of pressure and mass density changes.

TABLE 2. The table on the left is the regression analysis data of the maximum electron density and other variables, and the table on the right is the regression analysis data of the maximum electron density and other variables.

Ne max	t-value	p-value	Beta
P	1.32	0.235	165.5701
Mass Density	-1.31	0.237	-129.1184
T	-1.31	0.237	-67.03294
R-squared = 0.886		Adj R-squared = 0.829	

P	t-value	p-value	Beta
Mass Density	1773.66	0.000	165.5701
T	920.86	0.000	-129.1184
R-squared = 1.0000		Adj R-squared = 1.0000	

tal and material parameters. Key variables include pressure, mass density, and temperature. Pressure determines the forces between particles; mass density determines the number of particles per unit volume; and temperature indicates the thermal dynamics of the particles. Therefore, analyzing the changes in maximum electron density requires considering the interaction of these parameters and their overall effects. Fig. 6 illustrates the relationship between the maximum electron density and pressure, mass density, and temperature.

In Figs. 6(a), (b), and (c), the red lines represent the changing trend of maximum electron density along the transmission path, while the corresponding blue lines represent the changes in temperature, mass density, and pressure. All variable values have been normalized to eliminate dimensional effects, facilitating the analysis of the correlation between the changing trends of different influencing factors. It can be observed in Fig. 6 that the variation in SRV has a highly similar impact on pressure and maximum electron density, followed by mass density, with temperature showing the weakest correlation. Therefore, it can be inferred that the variation in SRV may affect the maximum electron density by changing the pressure.

In this study, the ideal gas equation was used to calculate pressure. The equation is given by $P = \rho RT$, where P (pressure) is a function of T (temperature), R (gas constant), and ρ (mass density), with R being a constant [39]. According to this equation, pressure changes are directly related to temperature and mass density. Fig. 6(d) compares the changing trends of pressure and mass density with varying SRV, with both variables being normalized. The changing trends of pressure and mass density are observed to be basically consistent. After preliminary analysis, regression analysis was performed on these variables, and the results are presented in Table 2.

In Table 2, the t-value serves as a statistical measure to evaluate the significance of sample data, representing the ratio of between-group differences to within-group differences. A larger t-value indicates a more significant difference. The p-value denotes the significance level of the statistical test, indicating the probability of the regression coefficient being significantly different from zero. The standard regression coefficient (Beta) reflects the degree of influence of the independent variable on the dependent variable after eliminating unit effects, with larger values indicating a greater impact of the factor on

the dependent variable. R-squared signifies the extent to which the variability of the dependent variable can be explained by the independent variables in the regression model, ranging from 0 to 1, with values closer to 1 indicating a better fit of the model. Adjusted R-square is the adjusted coefficient of determination, measuring the effect of adding explanatory variables on the R-square, with its value also ranging from 0 to 1, where a higher value indicates a better fit.

The table on the left of Table 2 presents regression data with maximum electron density as the dependent variable and pressure, mass density, and temperature as independent variables. The table shows that the significance levels for the three independent variables are all around 0.23, while the absolute value of the standardized regression coefficient (Beta) for pressure is the largest. This indicates that pressure has the most significant impact on maximum electron density, i.e., changes in pressure are the primary cause of changes in maximum electron density. Similar analysis applied to the table on the right of Table 2 reveals that changes in mass density drive variations in pressure. The R-squared values in both tables are close to 1, indicating a high level of fit between the model and the data. Therefore, it can be inferred that changes in SRV cause variations in mass density near the antenna, affecting pressure and leading to changes in maximum electron density along the transmission path.

On the other hand, in this study, numerical simulations were conducted using the fluid dynamics equations, with a key focus on utilizing the Naive-Stokes equation to describe fluid dynamic characteristics involving interactions among velocity, pressure, density, and viscosity. The mass equation in Formula (16) indicates a close connection between changes in mass density and gas flow velocity [40]. Typically, an increase in flow velocity in the plasma sheath region is accompanied by a decrease in mass density. When the pressure within a fluid element increases, the fluid moves towards the low-pressure area and accelerates. This change in velocity, in turn, affects pressure and mass density. Fig. 7 illustrates the variation in fluid velocity during the formation of the plasma sheath.

$$\frac{\partial \rho}{\partial t} + \nabla \cdot (\rho \vec{u}) = 0 \quad (16)$$

where ρ is the mass density, and \vec{u} is the velocity vector.

Figure 7 presents the velocity distribution calculated based on the fluid dynamics model. In the analysis, the velocity is divided into horizontal and vertical components. Figs. 7(a)–(c) and (d)–(f) depict the horizontal velocity in the early and late stages of the study, while panels (g)–(i) and (o)–(q) correspond to the vertical velocity in the early and late stages. In the distribution plots, the SRVs are arranged from left to right as 0.5, 1, and 10, with color depth representing the corresponding velocity magnitude. Fig. 7 shows that, whether V_x (horizontal velocity) or V_y (vertical velocity), the velocity distribution remains generally consistent throughout the process. However, the rightmost color bar in the figures exhibits different velocity values, and the variation in color intensity on the outer side of the sheath also indicates differences in velocity with size ratios. The results depicted in the figures illustrate that changes

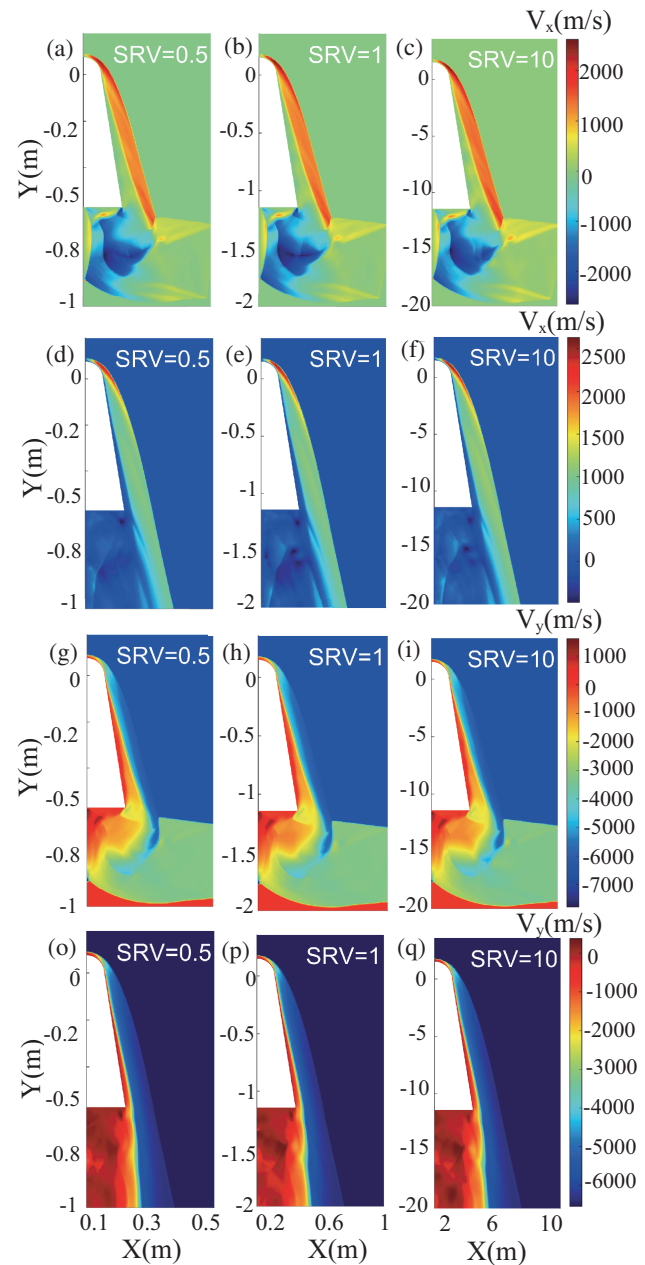


FIGURE 7. (a), (b), and (c) show early-stage horizontal velocity distributions for size ratios of 0.5, 1, and 10, respectively. (d), (e), and (f) depict late-stage horizontal velocity distributions for the same size ratios. (g), (h), and (i) display early-stage vertical velocity distributions, while (o), (p), and (q) exhibit late-stage vertical velocity distributions, all corresponding to size ratios of 0.5, 1, and 10.

in SRV have a notable impact on the magnitude of flow velocity, both in the horizontal and vertical directions. To clearly illustrate the relationship between pressure, mass density, and velocity trends, Fig. 8 provides a comparative analysis of numerical variations.

As shown in Fig. 8(a), the red line illustrates the variation in pressure with increasing SRV. In Fig. 8(b), the red line depicts the variation in mass density with increasing SRV, while the blue line reflects the trend of velocity near the transmission path under changing SRV. All variables have been normalized

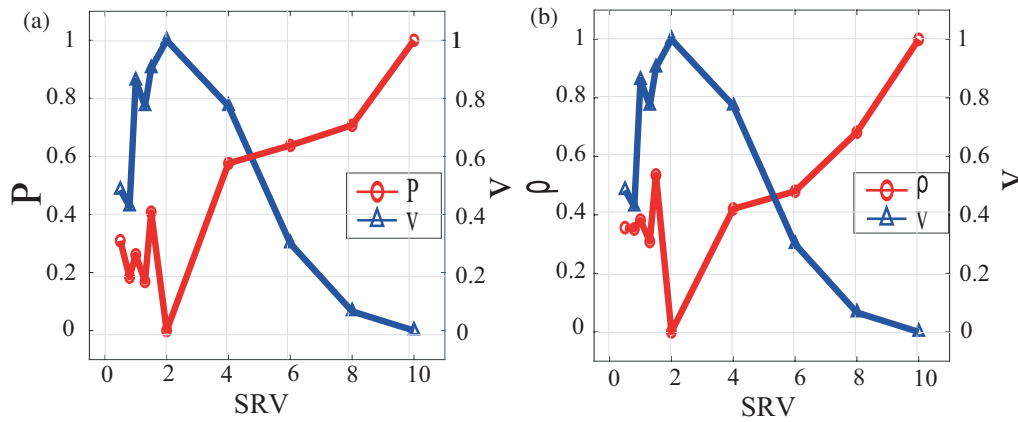


FIGURE 8. Comparative trends of (a) pressure and (b) mass density with velocity as SRV varies.

for analysis. Based on the analysis of Fig. 8, the velocity near the transmission path shows an opposite trend to the changes in pressure and mass density: as the SRV increases, the velocity decreases, while pressure and mass density increase. This phenomenon aligns with the physical laws described by the mass Equation (3).

After analyzing the impact of SRV on maximum electron density, the following conclusions can be drawn: as the SRV increases from small (ratio 0.5) to large (ratio 10), the maximum electron density exhibits unstable fluctuations and eventually tends to rise. This change in trend is caused by the interaction of fluid dynamic parameters (mass density, pressure, temperature, and velocity) influenced by changes in SRV, particularly the direct impact of fluid velocity changes on mass density, altering the pressure distribution, and consequently affecting electron density.

In the evolution of the plasma sheath, another parameter equally important as electron density is the collision frequency. To analyze its trend, the three peaks of collision frequency were studied, as shown in Fig. 9, depicting the relationship between collision frequency and SRV.

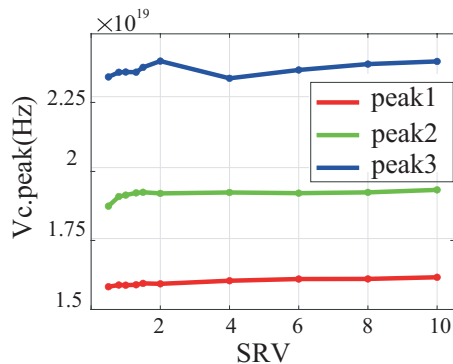


FIGURE 9. Variation in collision frequency along the transmission path with changing SRV.

As depicted in Fig. 9, the vertical axis represents the collision frequency along the transmission path. The red line corresponds to the first peak, the green line to the second peak,

and the blue line to the third peak. The study reveals that the SRV significantly influences the magnitude of the peaks. Regardless of the SRV, the third peak is consistently the largest, followed by the second peak and the first peak. Furthermore, as the SRV increases, the first and second peaks rise gradually, and the third peak exhibits fluctuations but generally shows an increasing trend.

3. THE IMPACT OF DIFFERENT-SIZED VEHICLE ON THE PROPAGATION OF TERAHERTZ SIGNALS

Within the plasma sheath, if the carrier frequency is lower than the maximum cutoff frequency, the signal will undergo total reflection. Terahertz signals range from 0.1 THz to 10 THz, providing an effective solution to overcome power outage problems.

The propagation characteristics of terahertz signals are affected by many factors such as electron density, thickness, collision frequency, and distribution shape in the plasma sheath. Research needs to use the data obtained from the numerical simulation in the previous section to analyze these effects. In addition, considering that the propagation of the terahertz frequency band in the atmosphere may be affected by water vapor, oxygen and other factors and produce significant attenuation at certain frequencies, the research focuses on the “atmospheric window” frequency range that has better propagation in the atmosphere. For electromagnetic waves in the 30 to 300 GHz band, 94 GHz, 140 GHz, and 225 GHz are mainly selected as the carrier frequencies of the terahertz communication system [41, 42].

The study also finds that since the terahertz wavelength is much smaller than the spatial scale of the inhomogeneity in the plasma sheath, this feature can be used to construct a one-dimensional non-uniform collision plasma model, and then carry out research on terahertz propagation in the plasma sheath [43]. Therefore, on this basis, the correlation coefficient can be calculated using the scattering matrix method (SMM), as shown in Fig. 10.

The plasma sheath, as illustrated in Fig. 10, is partitioned into N layers, where in the plasma parameters within each slender stratum exhibit uniformity. Assuming that the wave propagates

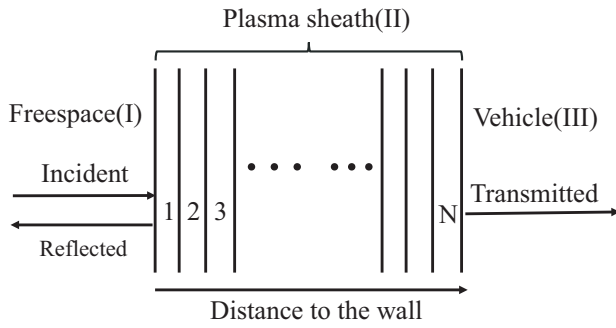


FIGURE 10. SMM schematic diagram.

along the x -axis, the incident wave enters the interface vertically from free space I. Eventually, in layer N , it transitions from the plasma region into free space III, corresponding to the region where the spacecraft is located. The recursive formula for the scattering matrix is as follows [28, 44]:

$$S_{\alpha} = \frac{1}{2K_x^{(\alpha)}} \begin{bmatrix} A & B \\ C & D \end{bmatrix} \quad (17)$$

$$A = \left(k_x^{(\alpha)} + k_x^{(\alpha-1)} \right) \exp \left[-j \left(k_x^{(\alpha-1)} - k_x^{(\alpha)} \right) d_{\alpha} \right] \quad (18)$$

$$B = \left(k_x^{(\alpha)} - k_x^{(\alpha-1)} \right) \exp \left[j \left(k_x^{(\alpha-1)} + k_x^{(\alpha)} \right) d_{\alpha} \right] \quad (19)$$

$$C = \left(k_x^{(\alpha)} - k_x^{(\alpha-1)} \right) \exp \left[-j \left(k_x^{(\alpha-1)} + k_x^{(\alpha)} \right) d_{\alpha} \right] \quad (20)$$

$$D = \left(k_x^{(\alpha)} + k_x^{(\alpha-1)} \right) \exp \left[j \left(k_x^{(\alpha-1)} - k_x^{(\alpha)} \right) d_{\alpha} \right] \quad (21)$$

where α denotes the N th layer. The global scattering matrix is computed according to the following expression:

$$S_g = \left(\prod_{\alpha=N}^2 S_{\alpha} \right) \frac{1}{2k_x^{(1)}} \begin{bmatrix} k_x^{(1)} - k_x^{(0)} & k_x^{(1)} + k_x^{(0)} \\ k_x^{(1)} + k_x^{(0)} & k_x^{(1)} - k_x^{(0)} \end{bmatrix} \quad (22)$$

The superscript 0 signifies free space (region I). Applying the electromagnetic field boundary conditions at the interface between regions II and III based on the medium interface, the recursive matrix expression can be formulated as follows:

$$S_g \begin{bmatrix} R \\ 1 \end{bmatrix} = V \cdot T \quad (23)$$

$$V = \frac{1}{2k_x^{(N_L)}} \begin{bmatrix} C \\ D \end{bmatrix} \quad (24)$$

$$C = \left(k_x^{(N_L)} + k_x^{(N_L+1)} \right) \times \exp \left[j \left(k_x^{(N_L)} - k_x^{(N_L+1)} \right) d_{N_L+1} \right] \quad (25)$$

$$D = \left(k_x^{(N_L)} - k_x^{(N_L+1)} \right) \times \exp \left[-j \left(k_x^{(N_L)} + k_x^{(N_L+1)} \right) d_{N_L+1} \right] \quad (26)$$

where the superscript N_L+1 denotes region III.

The power reflection coefficient, power transmission coefficient, and power absorption coefficient are obtained from the following expressions:

$$R_p = |R|^2 \quad (27)$$

$$T_p = |T|^2 \quad (28)$$

$$A_p = 1 - R_p - T_p \quad (29)$$

Utilizing the aforementioned SMM, the results can be computed across varying size ratios in Fig. 11.

Figs. 11(a), (b), and (c) depict the absorption, reflection, and transmission coefficients of terahertz signals (at 94 GHz, 140 GHz, and 225 GHz) for vehicles of different sizes. The enlargement of vehicle dimensions significantly enhances the absorption coefficient of terahertz signals, particularly evident in larger vehicle. For vehicle with size ratios less than 6, an increase in carrier frequency leads to a decrease in the absorption coefficient. Terahertz signal reflection coefficients exhibit irregular fluctuations in smaller vehicle, especially pronounced at 94 GHz. Among vehicles with size ratios between 2 and 10, larger vehicle exhibits higher reflection coefficients, which also decrease with an increase in carrier frequency. Transmission coefficients for all signals decrease with an increase in SRV, indicating a weakened transmission capability. For a vehicle exceeding a size ratio of 6, the transmission of signals at all frequencies is extremely weak. At higher carrier frequencies, signal transmission is enhanced.

In the course of this study, assuming a blackout threshold of $T_p = 0.15$, it is observed that there exists a safe upper limit for the ratio of spacecraft sizes when considering different carrier frequencies. This limit ensures the reliability of communication. Specifically, when the carrier frequency is 0.14 THz, the SRV should be controlled within 1.5; when the carrier frequency is 0.22 THz, the SRV should be limited to within 4. Therefore, to mitigate the blackout phenomenon, it is advisable to design vehicles with sizes kept within reasonable bounds. Simultaneously, increasing the signal frequency contributes to ensuring smooth communication.

Further analysis reveals the relationship between the attenuation coefficient of terahertz signal transmission and SRV, as depicted in Fig. 11(d). For vehicle at the same size, the attenuation is most significant at 94 GHz and minimal at 225 GHz. The attenuation of terahertz signal transmission gradually intensifies with the enlargement of the spacecraft size. One contributing factor is the enhanced energy absorption of carriers due to higher electron density or collision frequency, leading to increased energy loss. As mentioned earlier, electron density and collision frequency vary with changes in VS. Additionally, an increase in the thickness of the plasma sheath, proportional to SRV, alters the propagation path and time of electromagnetic waves, potentially intensifying absorption and scattering through thicker media, thereby increasing signal attenuation. Fig. 12 further validates the correlation between terahertz signal attenuation characteristics and changes in the thickness of the plasma sheath.

Figure 12 indicates that the signal attenuation coefficient linearly increases with the thickness of the plasma sheath envelope, following a similar pattern as in Fig. 11(d). This consistency implies that the enlargement of spacecraft size leads to an increase in the thickness of the plasma sheath along the transmission path, subsequently exacerbating signal attenuation. The thickening of the plasma sheath enhances the interaction frequency between terahertz waves and free electrons, re-

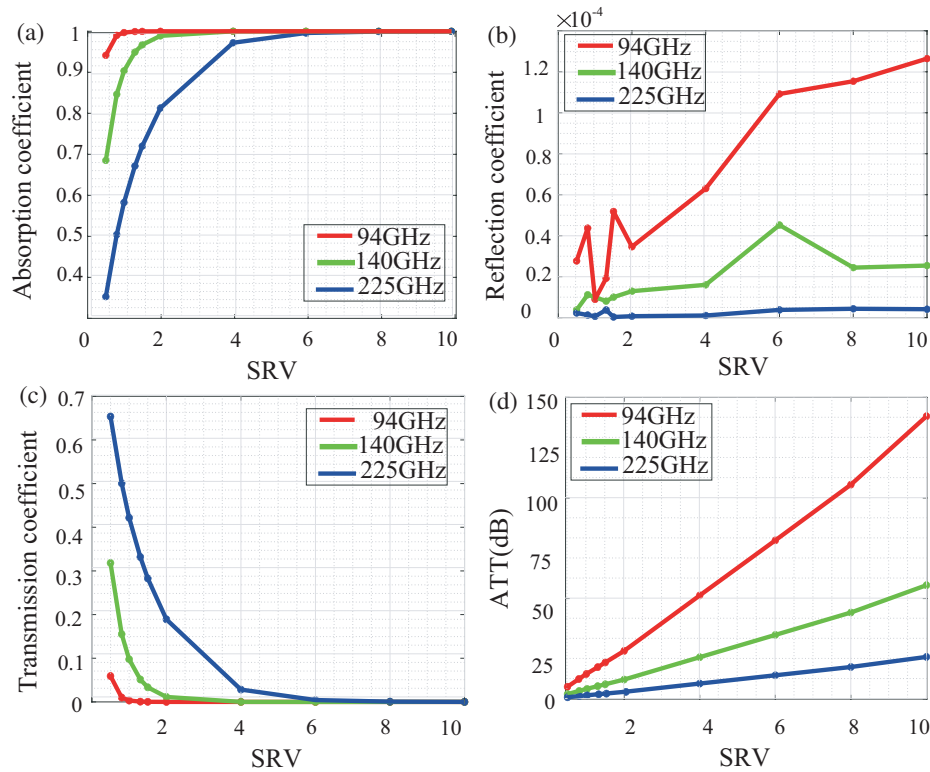


FIGURE 11. (a) absorption coefficient, (b) reflection coefficient, (c) transmission coefficient, and (d) attenuation coefficients of terahertz signals for spacecrafts of different sizes.

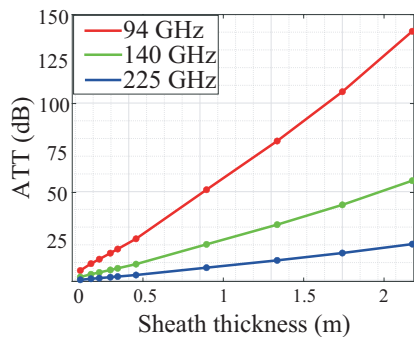


FIGURE 12. The relationship between the attenuation coefficient along the transmission path and the thickness of the sheath envelope for spacecrafts of different sizes.

sulting in a more pronounced loss of signal energy. The 94 GHz signal exhibits the maximum attenuation under a fixed thickness of the plasma sheath, while the attenuation of the 225 GHz signal is relatively minimal. The increase in sheath thickness emerges as the primary cause of signal attenuation. Consequently, in the construction of larger vehicle, adopting designs that minimize the thickness of the plasma sheath proves conducive to mitigating signal attenuation.

4. SUMMARY AND CONCLUSION

This study initially employed a hypersonic fluid dynamics model to analyze the structure of plasma sheath within vehicles

of various sizes. The research further investigated the propagation characteristics of terahertz signals within these sheaths.

The size of vehicle notably affects the plasma sheath parameters of a vehicle. Although SRV changes affect the wake region and sheath top, the sidewalls, particularly the rear one, remain stable, facilitating communication. The plasma sheath's thickness has a linear relationship with SRV. The electron density distribution along the transmission path follows a Gaussian pattern, unchanged by SRV variations and exhibits three peaks of increasing collision frequency. In smaller vehicles, an increased SRV causes unstable fluctuations in maximum electron density attributed to changes in velocity, mass density, and pressure distribution. A higher SRV results in the full absorption of terahertz signals, which is the principal cause of signal attenuation, accompanied by a minor increase in reflection and a reduction in transmission coefficients. At elevated carrier frequencies, absorption and reflection coefficients diminish, while transmission coefficients are enhanced. Increasing vehicle size increases plasma sheath thickness, leading to linear terahertz signal attenuation. Hence, for large vehicle, reducing the thickness of the plasma sheath helps reduce signal attenuation.

ACKNOWLEDGEMENT

This work was supported in part by the Natural Science Foundation of Jiangxi under Grant 20224BAB212027, in part by the Financial Contract of Science and Technology Project of Jiangxi Province under Grant ZBG20230418032, and in part by the Interdisciplinary Innovation Fund of Natural Science from Nanchang University under Grant 9167-28220007-YB2104.

REFERENCES

- [1] Rybak, J. P. and R. J. Churchill, "Progress in reentry communications," *IEEE Transactions on Aerospace and Electronic Systems*, Vol. AES-7, No. 5, 879–894, 1971.
- [2] Ding, Y., B. Bai, X. Li, G. Niu, and Y. Liu, "Research on EM shielding mechanism of the plasma-sheath-covered target," *IEEE Transactions on Plasma Science*, Vol. 51, No. 3, 632–640, 2023.
- [3] Leblanck, J. E. and T. Fujiwara, "Comprehensive analysis of communication with a reentry vehicle during blackout phase," *Japan Society for Aeronautical and Space Sciences, Transactions*, Vol. 39, No. 124, 211–221, 1996.
- [4] Yang, X., "Density oscillation of plasma sheath and its influence on electromagnetic wave behavior," *Journal of the Korean Physical Society*, Vol. 82, No. 12, 1150–1156, 2023.
- [5] Starkey, R. P., "Hypersonic vehicle telemetry blackout analysis," *Journal of Spacecraft and Rockets*, Vol. 52, No. 2, 426–438, 2015.
- [6] Amoroso, S., R. Bruzzese, N. Spinelli, and R. Velotta, "Characterization of laser-ablation plasmas," *Journal of Physics B: Atomic, Molecular and Optical Physics*, Vol. 32, No. 14, R131, 1999.
- [7] Hodara, H., "The use of magnetic fields in the elimination of the re-entry radio blackout," *Proceedings of the IRE*, Vol. 49, No. 12, 1825–1830, 1961.
- [8] Wu, X., J. Zhang, G. Dong, and L. Shi, "Characteristics of the electromagnetic wave propagation in the magnetized plasma sheath and the practical method for blackout mitigation," *Chinese Physics B*, Vol. 33, No. 5, 055201, 2024.
- [9] Meyer, J. W., "System and method for reducing plasma induced communication disruption utilizing electrophilic injectant and sharp reentry vehicle nose shaping," 2007.
- [10] Starkey, R., "Electromagnetic wave/magnetoactive plasma sheath interaction for hypersonic vehicle telemetry blackout analysis," in *34th AIAA Plasmadynamics and Lasers Conference*, 4167, Orlando, FL, USA, 2003.
- [11] Brandel, D. L., W. A. Watson, and A. Weinberg, "NASA's advanced tracking and data relay satellite system for the years 2000 and beyond," *Proceedings of the IEEE*, Vol. 78, No. 7, 1141–1151, 1990.
- [12] Li, J., Y. Pi, and X. Yang, "A conception on the terahertz communication system for plasma sheath penetration," *Wireless Communications and Mobile Computing*, Vol. 14, No. 13, 1252–1258, 2014.
- [13] Sun, S., S. Liu, and S. Zhong, "Analysis of terahertz wave penetration capacity to 2D conductive cylinder coated with steady-state parabolic distribution plasma media," *Results in Physics*, Vol. 27, 104516, 2021.
- [14] Zheng, L., Q. Zhao, S. Liu, X. Xing, and Y. Chen, "Theoretical and experimental studies of terahertz wave propagation in unmagnetized plasma," *Journal of Infrared, Millimeter, and Terahertz Waves*, Vol. 35, 187–197, 2014.
- [15] Dong, Q., Y. Han, and Q. Zhang, "Transmission characteristics of terahertz waves in a hypersonic target plasma sheath," *Chinese Journal of Quantum Electronics*, Vol. 40, No. 2, 258, 2023.
- [16] Zhang, J. and Y. Guohua, "Effect of random distribution of plasma on transmission characteristics of THz waves," *Journal of Northwest Normal University*, Vol. 58, 58–65, 2022.
- [17] Tian, Y., Y. Han, Y. Ling, and X. Ai, "Propagation of terahertz electromagnetic wave in plasma with inhomogeneous collision frequency," *Physics of Plasmas*, Vol. 21, No. 2, 023301, 2014.
- [18] Rao, Q., G. Xu, P. Wang, and Z. Zheng, "Study on the propagation characteristics of terahertz waves in dusty plasma with a ceramic substrate by the scattering matrix method," *Sensors*, Vol. 21, No. 1, 263, 2021.
- [19] Zhang, Y., G. Xu, and Z. Zheng, "Terahertz waves propagation in an inhomogeneous plasma layer using the improved scattering-matrix method," *Waves in Random and Complex Media*, Vol. 31, No. 6, 2466–2480, 2021.
- [20] Zhang, J., Y. Liu, X. Li, L. Shi, M. Yang, and B. Bai, "2D simulation of the electromagnetic wave across the non-uniform reentry plasma sheath with COMSOL," *AIP Advances*, Vol. 9, No. 5, 055316, 2019.
- [21] Yuan, K., Y. Wang, L. Shen, M. Yao, X. Deng, F. Zhou, and Z. Chen, "Sub-THz signals' propagation model in hypersonic plasma sheath under different atmospheric conditions," *Science China Information Sciences*, Vol. 60, 1–11, 2017.
- [22] Wei, C., L. Yang, Z. Huang, and L. Guo, "Research on the propagation characteristics of THz waves in spatial inhomogeneous and time-varying and weakly ionized dusty plasma," *IEEE Transactions on Plasma Science*, Vol. 47, No. 10, 4745–4752, 2019.
- [23] Chen, C., Y. Bai, J. Zhang, Y. Yang, and J. Wang, "Numerical study of oblique incidence of terahertz wave to magnetized plasma," *High Power Laser and Particle Beams*, Vol. 30, No. 1, 013 101–1, 2018.
- [24] Tang, R., M. Mao, K. Yuan, Y. Wang, and X. Deng, "A terahertz signal propagation model in hypersonic plasma sheath with different flight speed," *Physics of Plasmas*, Vol. 26, No. 4, 043509, 2019.
- [25] Guo, L., L. Guo, and J. Li, "Propagation of terahertz electromagnetic waves in a magnetized plasma with inhomogeneous electron density and collision frequency," *Physics of Plasmas*, Vol. 24, No. 2, 022108, 2017.
- [26] Ouyang, W., Q. Liu, and Z. Wu, "Difference analysis in terahertz wave propagation in thermochemical nonequilibrium plasma sheath under different hypersonic vehicle shapes," *Chinese Journal of Aeronautics*, Vol. 36, No. 10, 137–151, 2023.
- [27] Kundrapu, M., J. Loverich, K. Beckwith, P. Stoltz, A. Shashurin, and M. Keidar, "Modeling radio communication blackout and blackout mitigation in hypersonic vehicles," *Journal of Spacecraft and Rockets*, Vol. 52, No. 3, 853–862, 2015.
- [28] Hu, B. J., G. Wei, and S. L. Lai, "SMM analysis of reflection, absorption, and transmission from nonuniform magnetized plasma slab," *IEEE Transactions on Plasma Science*, Vol. 27, No. 4, 1131–1136, 1999.
- [29] Dunn, M. G. and S. Kang, "Theoretical and experimental studies of reentry plasmas," NASA, Tech. Rep., 1973.
- [30] Harloff, G. J. and B. M. Berkowitz, "HASA: Hypersonic aerospace sizing analysis for the preliminary design of aerospace vehicles," NASA, Tech. Rep., 1988.
- [31] Foias, C., O. P. Manley, R. Temam, and Y. M. Treve, "Asymptotic analysis of the navier-Stokes equations," *Physica D: Non-linear Phenomena*, Vol. 9, No. 1-2, 157–188, 1983.
- [32] Bhattacharyya, S., S. Minwalla, and S. R. Wadia, "The incompressible non-relativistic Navier-Stokes equation from gravity," *Journal of High Energy Physics*, Vol. 2009, No. 08, 059, 2009.
- [33] Anguiano, M., J. L. Egido, and L. M. Robledo, "Particle number projection with effective forces," *Nuclear Physics A*, Vol. 696, No. 3-4, 467–493, 2001.
- [34] Gupta, R. N., J. M. Yos, R. A. Thompson, and K.-P. Lee, "A review of reaction rates and thermodynamic and transport properties for an 11-species air model for chemical and thermal nonequilibrium calculations to 30000 K," NASA, Tech. Rep.,

- 1990.
- [35] Eymard, R., T. Gallouët, and R. Herbin, "Finite volume methods," *Handbook of Numerical Analysis*, Vol. 7, 713–1018, 2000.
- [36] Moukalled, F., L. Mangani, M. Darwish, F. Moukalled, L. Mangani, and M. Darwish, *The Finite Volume Method*, Springer, 2016.
- [37] Bachynski, M. P., T. W. Johnston, and I. P. Shkarofsky, "Electromagnetic properties of high-temperature air," *Proceedings of the IRE*, Vol. 48, No. 3, 347–356, 1960.
- [38] Goebel, D. M., I. Katz, and I. G. Mikellides, *Fundamentals of Electric Propulsion*, John Wiley & Sons, 2023.
- [39] Martin, J. J. and Y.-C. Hou, "Development of an equation of state for gases," *AIChE Journal*, Vol. 1, No. 2, 142–151, 1955.
- [40] Chorin, A. J., "Numerical solution of the navier-stokes equations," *Mathematics of Computation*, Vol. 22, No. 104, 745–762, 1968.
- [41] Liebe, H., "Atmospheric EHF window transparencies near 35, 90, 140 and 220 GHz," *IEEE Transactions on Antennas and Propagation*, Vol. 31, No. 1, 127–135, 1983.
- [42] Cao, X.-C., J.-H. Hao, Q. Zhao, F. Zhang, J.-Q. Fan, and Z.-W. Dong, "Analysis of high-frequency atmospheric windows for terahertz transmission along Earth-space paths," *IEEE Transactions on Antennas and Propagation*, Vol. 70, No. 7, 5715–5724, 2022.
- [43] Sun, J., Y. Zheng, J. Shi, Y. Zhao, Y. Li, D. Wu, H. Cai, X. Zhang, X. Zhu, Y. Liu, *et al.*, "Propagation characteristics of terahertz wave in inductively coupled plasma," *Optics Express*, Vol. 29, No. 22, 35 837–35 847, 2021.
- [44] Tang, D. L., A. P. Sun, X. M. Qiu, and P. K. Chu, "Interaction of electromagnetic waves with a magnetized nonuniform plasma slab," *IEEE Transactions on Plasma Science*, Vol. 31, No. 3, 405–410, 2003.